

# Nanocrystalline Powder Cores for High-Power High-Frequency Power Electronics Applications

Chaoqiang Jiang, *Member, IEEE*, Xinru Li, *Student Member, IEEE*, Saikat S. Ghosh, *Student Member, IEEE*, Hui Zhao, *Member, IEEE*, Yanfeng Shen, *Member, IEEE*, Teng Long, *Member, IEEE*

**Abstract**—Soft magnetic composites (SMCs) based magnetic cores are attractive in high frequency inductor design. The desired overall core permeability of SMC core can be achieved by adjusting the powder size, addition of insulation material and phosphoric acid, and pressure during the preparation process to reduce the air gap loss and ease the inductor design. The nanocrystalline alloy (Fe-Cu-Nb-Si-B) is an emerging SMC with high saturation flux density and low hysteresis loss, showing potential suitability for SMC based magnetic cores. To date, nanocrystalline alloys are mostly used in form of laminated ribbon for magnetic cores and nanocrystalline powder SMCs have been seldom used in practice. Also, neither experimental validation nor comparison with other commercialized and commonly used SMC cores has been reported. In this paper, the structure and manufacturing process of nanocrystalline powder cores are introduced. The calculation of core loss is defined for the nanocrystalline powder core. The characteristics and performance of the nanocrystalline powder toroidal core are compared with those of existing commercial SMC cores such as Fe-Si powder (X flux), Fe-Ni powder (High flux), Fe-Si-Al powder (Kool M $\mu$ ), Fe-Ni-Mo powder (MPP). Experimental results are conducted at frequencies from 100 kHz to 600 kHz to verify the loss calculation and feasibility of this new nanocrystalline powder core.

**Index Terms**— Nanocrystalline powder core, toroidal inductor, core loss, high frequency magnetics, soft magnetic composites.

## I. INTRODUCTION

**D**UE to the rapid development of power electronics applications especially for the dual active bridge converter [1-3], wireless power transfer [4-6], and electric vehicle (EV) tractions and charging [7-9], high frequency and high power magnetic components have become the key to further improvement of the power density and system efficiency [10].

To date, ceramic ferrites have been the most commonly used magnetic cores in high power and high frequency inductors due to the lower cost and relatively lower core loss than silicon steel at high operating frequencies, normally above 100 kHz [11]. However, the ferrite cores saturate at a much lower magnetic

flux density level, normally between 0.2-0.5 T. In addition, the embrittlement of ferrite cores makes them prone to mechanical breakage. In order to improve the saturation flux density with higher permeability, Hitachi Metals developed the first nanocrystalline soft magnetic material, named Finemet. The Finemet is with high saturation flux density, high permeability, and stable temperature characteristics. However, inductors using the Finemet alloy must have discrete airgaps between more than one piece of cores to reduce the overall permeability of the core and it is challenging to have Finemet cores for some applications with high DC bias current due to saturation from high permeabilities. The powder cores with distributed air gaps inherently have low permeabilities without using multiple pieces of cores to create discrete airgaps for high DC bias current [12]. Generally, air gaps need to be added in ferrite core based inductors to reduce the effective permeability of the core and then to reduce the flux density [13], which will induce additional power loss due to fringing flux around air gaps and the complexity of the inductor structure and design [14].

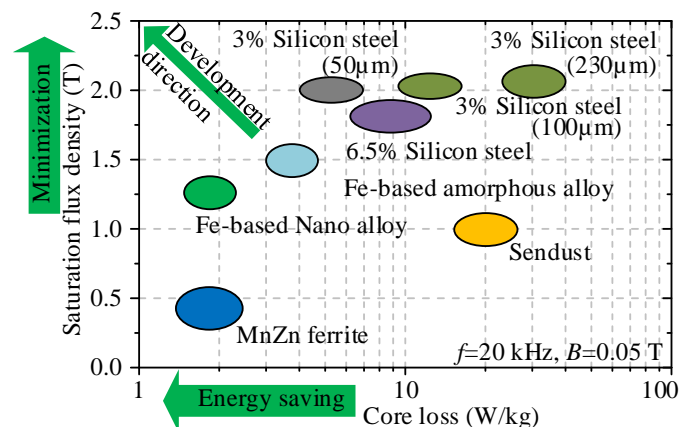


Fig. 1. Development trend of soft magnetic materials.

In order to achieve adjustable permeability, higher saturation flux density and lower core loss at the high operating frequencies, the soft magnetic composites (SMCs), also known as soft magnetic powder cores, have become increasingly popular based on well-developed powder metallurgy [15]. The distributed micro air gaps formed by the binding materials (a minimum amount around 2-5 weight %) are adopted to reduce the permeability of powder cores. The aim is to achieve a high DC offset of average flux density caused by the high DC current

Manuscript received September 25, 2019; revised December 16, 2019; accepted March 3, 2020. (Corresponding author: Teng Long).

The authors are with the Department of Engineering-Electrical Engineering Division, University of Cambridge, Cambridge CB3 0FA, U.K. (e-mail: cj426@cam.ac.uk, xl418@cam.ac.uk, ssg39@cam.ac.uk, hz352@cam.ac.uk, ys523@cam.ac.uk, tl322@cam.ac.uk).

TABLE I. COMPARISON OF MAGNETIC MATERIALS PROPERTIES

Material	Structure	Saturation flux density $B_{max}$ (T)	Coercive force $H_c$ (A·m <sup>-1</sup> )	Relative permeability $\mu_r$	Resistivity $\rho$ ( $\mu\Omega\cdot m$ )	Curie temperature $T_c$ (°C)	Core loss (kW/m <sup>3</sup> )@0.2 T, 100kHz	Thickness $t$ ( $\mu m$ )
Mn-Zn 3C94	Ceramic Ferrite	0.47	17.4	2300	$5\times 10^6$	220	384.62	Bulk
Fe <sub>73.5</sub> Cu <sub>1</sub> Nb <sub>3</sub> Si <sub>13.5</sub> B <sub>9</sub>	Nanocrystalline	1.24	0.5	100000	1.18	600	279.30	18
Fe <sub>73.5</sub> Cu <sub>1</sub> Nb <sub>3</sub> Si <sub>15.5</sub> B <sub>7</sub>	Nanocrystalline	1.23	0.4	110000	1.15	600	257.35	21
Fe <sub>76</sub> (SiB) <sub>24</sub>	Amorphous	1.45	3.0	8000	1.35	420	364.96	23
Co <sub>68</sub> Fe <sub>4</sub> (MoSiB) <sub>28</sub>	Amorphous	0.55	0.3	150000	1.35	240	269.23	23
80% Ni-Fe	Crystalline	0.75	0.5	100000	0.55	360	783.37	50
50%-60% Ni-Fe	Crystalline	1.55	5.0	40000	0.45	440	1650.17	70

for high power DC-DC converters. The binders provide insulating coatings for the ferromagnetic powder particles, which are served as barriers to isolate the global eddy current paths [16]. As each powder particle is segregated by the binding material, the eddy current path between particles is eliminated, hence the eddy current loss can be minimized. Meanwhile, the binders also act as lubricants during the compressing process as well as increasing the mechanical strength and reducing the brittleness. As a result, SMCs exhibit high flux density, lower core losses and reliable mechanical properties, which are promising candidates for high-frequency magnetic components, particularly for DC inductors [17].

Nanocrystalline alloy ribbons have been used to tape-wound C cores for high power inductors. Discrete air gaps are inevitable for the nanocrystalline ribbon C cores due to the high permeability of nanocrystalline ribbons. Although laminated ultra-thin nanocrystalline ribbons reduce the eddy current losses at the main body of the C cores, the airgap losses at the edge of two discrete air gaps are high due to the high conductivity of nanocrystalline materials [18].

With regard to the composition of the powder cores, there are mainly four powder cores have been commercialized in industry, namely, Fe-Si powder (X flux core), Fe-Ni powder (High flux core), Fe-Si-Al powder (Kool Mμ Max core), Fe-Ni-Mo powder (MPP core). When comparing the aforementioned alloys, the nanocrystalline alloy (Fe-Cu-Nb-Si-B) as a type of high performance soft magnetic material, can be mashed into microscale powders and compressed into magnetic cores. The nanocrystalline powder materials have been investigated in terms of losses, composition adjustment and manufacturing process for the potential use as magnetic cores [19-22]. However, investigation of constructed nanocrystalline powder cores in power electronics applications has been seldom reported. Neither experimental validation nor comparison with other commercialized SMC cores has been reported.

In this paper, a newly constructed nanocrystalline powder toroidal core is presented and experimentally investigated. The nanocrystalline powder core is fabricated by Advanced Technology & Materials Co., Ltd and is ready to put on the commercial market. The core loss calculation of this nanocrystalline powder core is derived and validated. Considering another four commonly powder cores, X-Flux core

(Fe-Si), High-Flux core (Fe-Ni), Kool-Mμ Max core (Fe-Si-Al) and MPP core (Fe-Ni-Mo), the contributions are listed as follows:

- 1) The DC bias performance of nanocrystalline is evaluated with magnetizing fore from 1 A/cm to 105 A/cm;
- 2) The core losses and B-H curves are conducted to compare the five powder cores from 100 kHz to 600 kHz.
- 3) The core loss model of the nanocrystalline powder core is determined and validated;
- 4) The thermal performances are analyzed at different operating frequencies.

In Section II, the development of nanocrystalline powder core including the manufacturing process is introduced. The core loss calculation of the nanocrystalline powder toroidal inductor is introduced and discussed. In Section III, the permeability under different DC biases is presented. In Section IV, an experimental prototype is constructed and tested to verify the core losses of different powder cores with the sinusoidal AC excitation current. The conclusion is drawn in Section V.

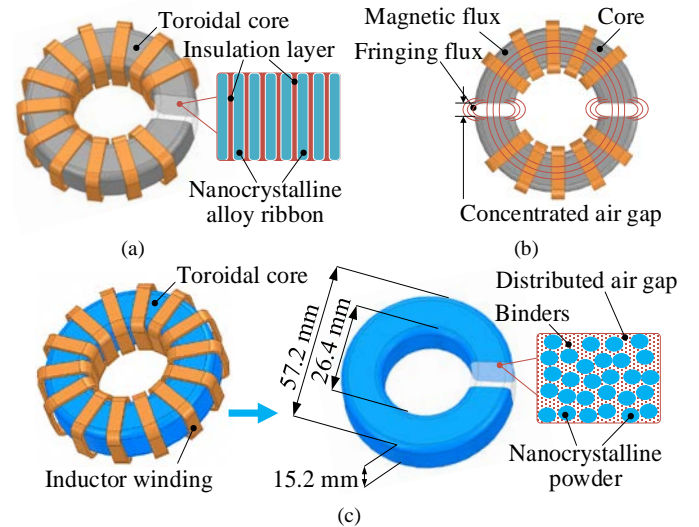


Fig. 2. Nanocrystalline core with different structures. (a) Toroidal core with nanocrystalline alloy ribbon. (b) Separated cores with concentrated air gaps. (c) Proposed new toroidal core with distributed air gaps formed by binder.

TABLE II MAGNETIC MATERIAL PROPERTIES FROM SEVERAL MANUFACTURERS

Manufacturer	Product name	Material composition	Saturation flux density $B_{sat}$ [T]	Curie temperature $T_c$ (°C)	Relative permeability $\mu_r$
AT&M Corp.	MGMP	Fe-Cu-Nb-Si-B	1.0	570	60
Magnetics	Kool M $\mu$	Fe-Al-Si	1.0	500	14-125
Magnetics	XFlux	Fe-Si	1.6	700	26-90
Magnetics	High Flux	Fe-Ni	1.5	500	14-160
Magnetics	MPP	Fe-Ni-Mo	0.8	460	14-550
Magnetics	Amoflux	Fe-Si-B	1.5	400	60
CSC	Sendust	Fe-Al-Si	1.0	500	26-125
CSC	Mega Flux	Fe-Si	1.6	700	26-90
CSC	High Flux	Fe-Ni	1.5	500	26-160
CSC	MPP	Fe-Ni-Mo	0.7	450	14-200
Micrometals	Mix-52	Fe	1.85	<770	75

## II. DEVELOPMENT OF NANOCRYSTALLINE CORE

As shown in Fig. 1, the development direction of the soft magnetic materials tends to be more energy-saving and size minimization. With regard to the flux density and core losses, the Fe-based alloy shows more potentials to be meet higher performance demands.

### A. Nanocrystalline SMC

Soft magnetic nanocrystalline alloys are referred to alloys that have a majority of grain diameters in the typical range from 1-50 nm, which are extremely fine compared to conventional crystalline soft magnetic materials like permalloys. The precursor of nanocrystalline alloys are amorphous alloys, and the nanocrystalline state is achieved by annealing amorphous alloys above the crystalline temperature. The first report of nanocrystalline alloys were Fe-Cu-Nb-Si-B alloys, which were developed in 1988 [23] and then the nanocrystalline SMC cores were fabricated in 1999 [24]. It was found that with a small addition of Cu and Nb, Fe-Cu-Nb-Si-B alloys exhibit ultrafine grain structure of body-centered cubic (BCC) Fe-Si with typically 10-15 nm grain size embedded in an amorphous matrix. The magnetic materials properties comparison of ferrite, nanocrystalline alloys, amorphous alloys and crystalline alloys are listed in Table I [25]. It can be found that the properties of nanocrystalline alloys are a unique combination of the low core loss, low coercive force, high permeability and high saturation flux density, which allows for further reducing size and weight of magnetic components in high power converters with working frequency up to 100 kHz.

Conventionally, the nanocrystalline core is formed by laminated ultra-thin (between 14 to 22  $\mu$ m) nanocrystalline ribbons as shown in Fig. 2 (a). The eddy current at the main body of the core is insignificant due to the lamination. The concentrated gaps should be placed to reduce the overall permeability of the core to avoid magnetic saturation as shown in Fig. 2 (b). However, the fringing flux will be produced among the two concentrated air gaps. Due to the high conductivity of nanocrystalline, higher eddy current loss will be generated at the air gaps. To reduce the air gap loss and maintain reduced permeability, the nanocrystalline alloy is

crushed into very fine particles and each particle is surrounded with air gaps formed by binders, as shown in Fig. 2 (c). The powders and binders are formed into one single piece of the toroidal core without concentrated large air gaps so the air gap loss is reduced.

### B. Manufacturing of the New Nanocrystalline Powder Core





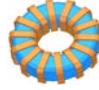
During the manufacturing process of the nanocrystalline powder, melt-spun  $\text{Fe}_{73.5}\text{Cu}_1\text{Nb}_3\text{Si}_{15.5}\text{B}_7$  (at. %) amorphous ribbons with 20  $\mu$ m thickness were embrittled by preheating at 350 °C for 1 hour in nitrogen atmosphere. The embrittled amorphous ribbons were pulverized by mechanical crushing to obtain flake-shaped fine amorphous powders [26]. Afterward, the grinded powders were sieved by screen and then particles with the size between 30 to 150  $\mu$ m were chosen. If the particles are too small the core will have poor flowability and magnetic properties, and it is difficult to compact the particles into cores if the particles are too large. Then, the sieved amorphous powders were passivated by 0.2 wt.% phosphoric acid at 75 °C to obtain uniformed phosphine oxide layer on the particle surface to reduce the eddy current loss.

After that, the passivated powders are mixed with organic binder (cyanate resin solution diluted by acetone), inorganic binder (glass powder) and lubricant, followed by cold compaction at a pressure of 2.1 GPa to form the toroidal shape core. The prepared cores with 57.2 mm in outer diameter, 26.4 mm in inner diameter and 15.2 mm in height are then annealed at 480 °C to relieve the stress and 580 °C to form nanocrystalline structure. After annealing, the powder cores are coated by epoxy resin at the core surface to finish off.

### C. Inductance of Toroidal Core Based inductors

The inductor core should have high saturation flux density in accordance with low permeability to accommodate high current [27, 28]. Although high permeability is beneficial in terms of increasing the inductance value, the core can saturate with lower current, which limits the power rating of the inductor. Thus, low permeability of the entire core is normally used for inductor, which is achieved by adding discrete or distributed air gaps. Meanwhile, the ripple current at high frequency also requires the magnetic material to have low hysteresis losses.

TABLE III. SPECIFICATIONS OF FIVE POWDER CORES COMPARED IN THIS PAPER

Items	Kool Mu	High flux	X Flux	MPP	Nanocrystalline powder
Coating color and shape					
Material	Fe-Si-Al	Fe-Ni	Fe-Si	Ni-Fe-Mo	Fe-Cu-Nb-Si-B
Core type	Powder core	Powder core	Powder core	Powder core	Powder core
Size (mm)	57.2×26.4×15.2	57.2×26.4×15.2	57.2×26.4×15.2	57.2×26.4×15.2	57.2×26.4×15.2
Bare volume $V$ (mm <sup>3</sup> )	28600	28600	28600	28600	28600
Cross section $A_c$ (mm <sup>2</sup> )	229	229	229	229	229
Path length $l_e$ (mm)	125	125	125	125	125
Relative permeability $\mu_r$	60	60	60	60	60
Air gap	Distributed	Distributed	Distributed	Distributed	Distributed
Winding (litz wire)	32*0.20 mm	32*0.20 mm	32*0.20 mm	32*0.20 mm	32*0.20 mm
Number of turns	42	42	42	42	42
Inductance $L_T$ (μH@100kHz)	244.1	243.4	238.5	243.6	243.8

The relative permeability of 60 is selected for the nanocrystalline powder core and other cores compared in this paper. Generally, the relative permeability is varied with the operating frequency. However, for this kind of powder cores with low relative permeability. The variation is less than 1% when the operating frequency is under 500 kHz except that X flux core is with 2.8% variation. Thus, the variation is negligible in this paper. Apart from the nanocrystalline powder core, the other four commonly used powder cores are listed in Table II from Magnetics and CSC. Also, comparisons between the nanocrystalline powder core and other commonly used magnetic powder cores are listed in Table III. All cores are in the standard toroidal shape as shown in Fig. 2. In order to reduce the skin effect and then the AC resistance at the high operating frequency, the Litz wire with 0.2 mm × 32 turns is adopted. Generally, the inductance  $L_T$  with turns of  $N_T$  can be calculated as:

$$L_T = \frac{\mu_r \mu_0 A_c N_T^2}{l_e} \quad (1)$$

where  $\mu_r$  is the relative permeability of the core,  $\mu_0$  is the permeability of free space,  $A_c$  is the cross-section area of the core,  $l_e$  is the effective magnetic path length.

#### D. Core Loss Model of Nanocrystalline Powder Inductor

One of the main concerns of the inductor is the core loss under the high frequency operation. In order to calculate the core loss mathematically, there is a commonly used Steinmetz equation to evaluate the core loss as:

$$P_V = k_i f^\alpha B^\beta \quad (2)$$

where  $P_V$  is the loss densities in kW/m<sup>3</sup>,  $f$  is the frequency in kilohertz,  $B$  is the flux density in Tesla,  $k_i$ ,  $\alpha$  and  $\beta$  are coefficients determined by the core materials and structure.

Based on the basic Steinmetz equation, an improved generalized Steinmetz equation (iGSE) [29, 30] was proposed to extend the available operating frequency and flux density range. The iGSE is expressed as:

$$P_V = \frac{1}{T} \int_0^T k_{iGSE} \left| \frac{dB}{dt} \right|^\alpha (\Delta B)^{\beta-\alpha} dt \quad (3)$$

where  $\Delta B$  is the peak-to-peak flux density and

$$k_{iGSE} = \frac{k_i}{(2\pi)^{\alpha-1} \int_0^{2\pi} |\cos \theta|^\alpha 2^{\beta-\alpha} d\theta} \quad (4)$$

For the nanocrystalline powder core with the relative permeability of 60, a set of experimental results has been adopted to determine the Steinmetz parameters in part IV.

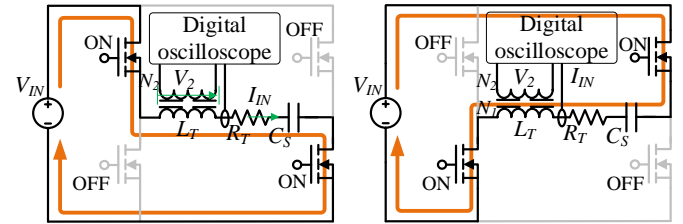


Fig. 3. Fundamental AC resonant test circuit at different switching statuses.

#### E. B-H Curve Measurement

In order to analyze the property of magnetic hysteresis and evaluate the core loss, the B-H loop needs to be measured. The test circuit is shown in Fig. 3. There are two windings wound on the core under test: primary winding with turns of  $N_1$  and secondary winding with turns of  $N_2$ . By measuring the secondary winding's open-circuit output voltage  $V_2$  and the primary winding's current  $I_{IN}$ , the magnetic field strength  $H$  and the flux density  $B$  can be expressed [31]:

$$H(t) = \frac{N_1 \cdot I_{IN}(t)}{l_e} \quad (5)$$

$$B(t) = \frac{1}{N_2 A_c} \int_0^T V_2(t) dt \quad (6)$$

Thus, the core loss  $P_V$  can be calculated as:



$$\begin{aligned}
 P_V &= f \cdot V \cdot \oint H dB \\
 &= f \cdot A_c \cdot I_e \cdot \int_0^T \frac{N_1 \cdot I_{IN}(t)}{l_e} \cdot \frac{1}{N_2 A_c} V_2(t) dt \\
 &= f \cdot \frac{N_1}{N_2} \int_0^T I_{IN}(t) \cdot V_2(t) dt
 \end{aligned} \quad (7)$$

Based on (7), the core loss can be measured in a digital oscilloscope by integrating the product of the secondary output voltage and the primary winding current. Besides, the B-H curve can be plotted by using the X-Y display of the oscilloscope after the calculations based on (5) and (6).

### III. PERMEABILITY MEASUREMENT WITH DC BIAS

The DC bias performance is measured by the LCR meter (Agilent E4980A) in series with two external DC current sources (Agilent 42841A). As a result, Fig. 4 shows the relationship between the permeability percentage of these five powder cores and the magnetizing force. It can be found that the permeability of all powder cores decreases with the increase of the magnetic field strength. The permeability of the nanocrystalline powder core shows the fastest decrease, and the permeability of X Flux core has the lowest decrease.

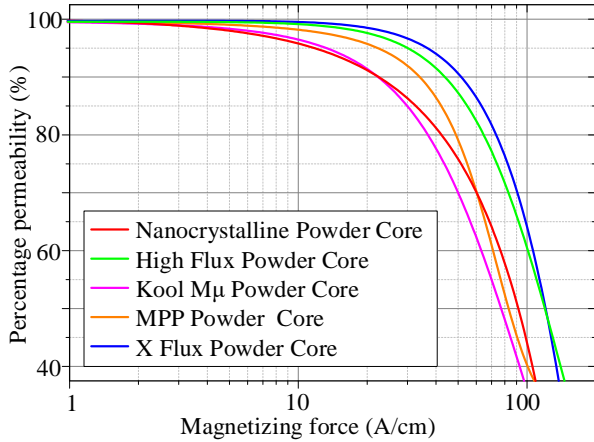


Fig. 4. Percentage permeability of tested powder cores with respect to magnetic field strength.

When there is a 10% reduction of permeability, it takes a magnetic field strength of 22.4 A/cm, 22.4 A/cm, 33.8 A/cm, 43.4 A/cm and 51.4 A/cm for nanocrystalline powder core, Kool Mμ core, MPP core, high flux core and X flux core, respectively. Then the dropping rate of the nanocrystalline powder core is relatively slow, where it shares the same 30% permeability reduction with MPP core at  $H = 60$  A/cm. When the magnetic field strength is larger than 60 A/cm, the most rapid permeability decrement is found for Kool Mμ core, followed by MPP core, nanocrystalline powder core, high flux core, and X flux core. The permeability reduction rate of high flux core is higher than that of X flux core when the magnetic field strength is larger than 103 A/cm with corresponding to a 50% permeability drop.

### IV. EXPERIMENTAL RESULTS OF CORE LOSS

In this part, the experimental comparisons of five powder cores listed in Table III, Kool Mμ core, high flux core, X flux core, MPP core, and nanocrystalline core, are conducted on the core loss measurement with DC suspended sinusoidal AC excitation and the thermal effect.

#### A. Core Loss under Sinusoidal AC Excitation

In order to verify the core loss under high frequency AC current, an AC resonant circuit is built as shown in Fig. 3, where a compensated capacitor is connected in series with the inductor. The compensated capacitor is to constitute an LC resonant tank to reduce the reactive power in the inductor test circuit and to create the sinusoidal excitation current at required frequencies with negligible harmonics. This resonant inverter is built to further test the five cores with higher input AC current and then achieve DC suspended core loss. The measured core losses include hysteresis loss and eddy current loss. When the operating frequency is high, the eddy current loss will be significant due to the low electrical resistivity of nanocrystalline alloy [32].

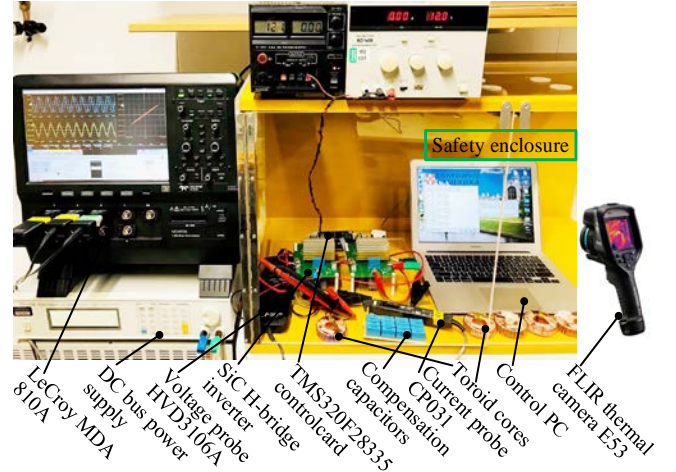


Fig. 5. Experimental setup of core loss measurement with DC suspended sinusoidal AC excitation.

As shown in Fig. 5, the Chroma 62024P-40-120 is used as the DC power supply for the inverter. The Teledyne LeCroy MDA810A oscilloscope (1 GHz, 8 Channels, 10 GS/s) is used to measure and display current, voltage, and B-H waveforms. The current probe and the voltage probe are Teledyne LeCroy CP031 and Teledyne LeCroy HVD3106A, respectively. The TMS320F28335 control card is used to drive the two SiC half-bridge inverters. The Litz wire (0.2 mm × 32 turns) is adopted for all cores to reduce the skin and proximity effects. In order to get higher AC current in the inductor with approximate 244 μH, various compensation capacitor arrays are used to achieve resonances at selected frequencies from 100 kHz to 600 kHz.

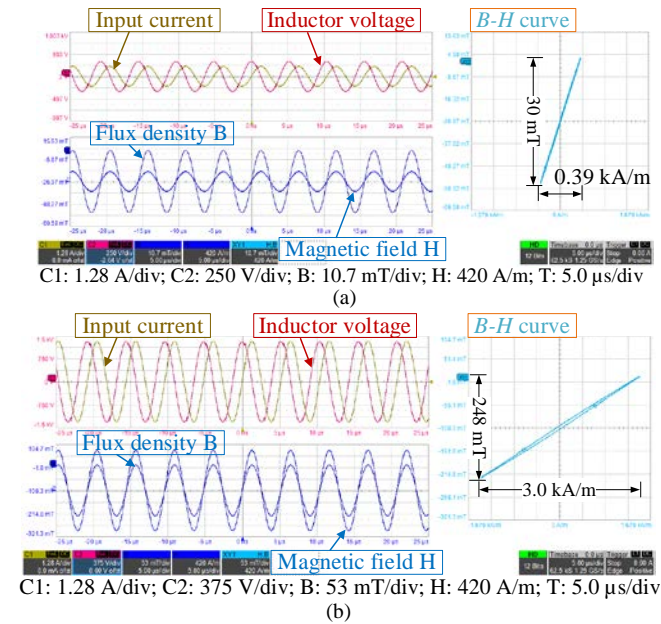


Fig. 6. Measured waveforms of nanocrystalline powder core with the operating frequency of 200 kHz. (a) 2.26 A peak-to-peak AC excitation current. (b) 9.1 A peak-to-peak AC excitation current.

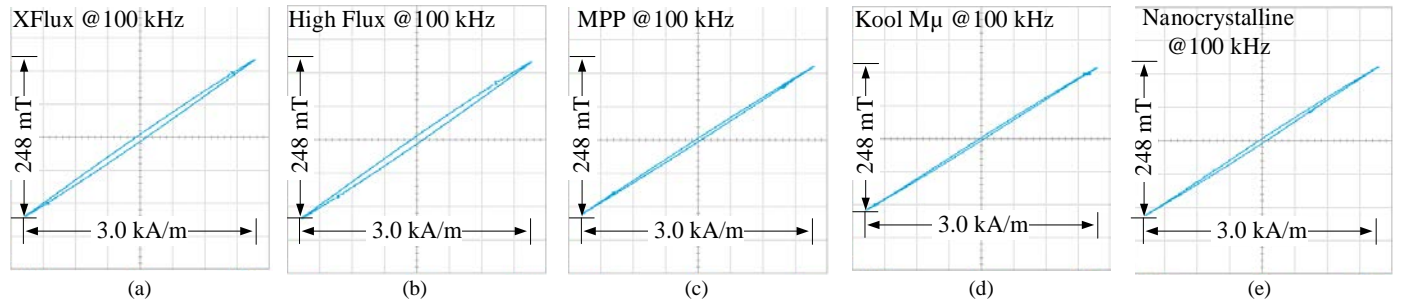


Fig. 7. Measured B-H curves with flux density of 248 mT under the frequency of 100 kHz. (a) X flux powder core. (b) High flux powder core. (c) MPP powder core. (d) Kool Mμ powder core. (e) Nanocrystalline powder core.

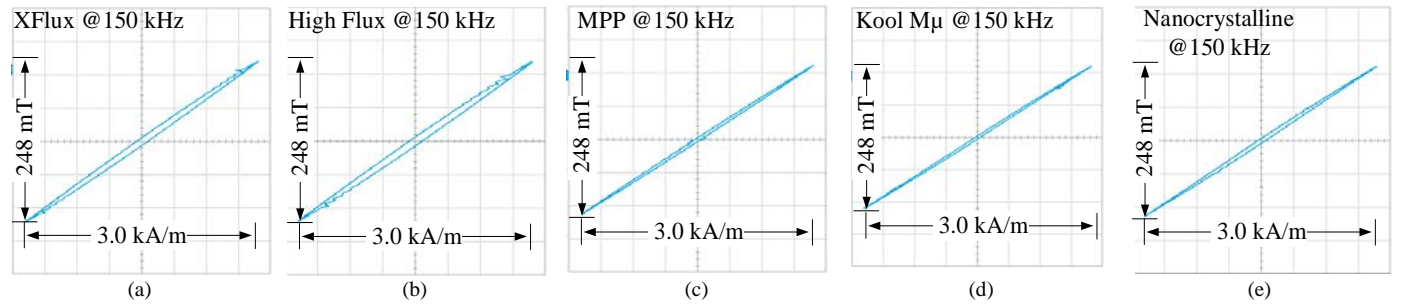


Fig. 8. Measured B-H curves with flux density of 248 mT under the frequency of 150 kHz. (a) X flux powder core. (b) High flux powder core. (c) MPP powder core. (d) Kool Mμ powder core. (e) Nanocrystalline powder core.

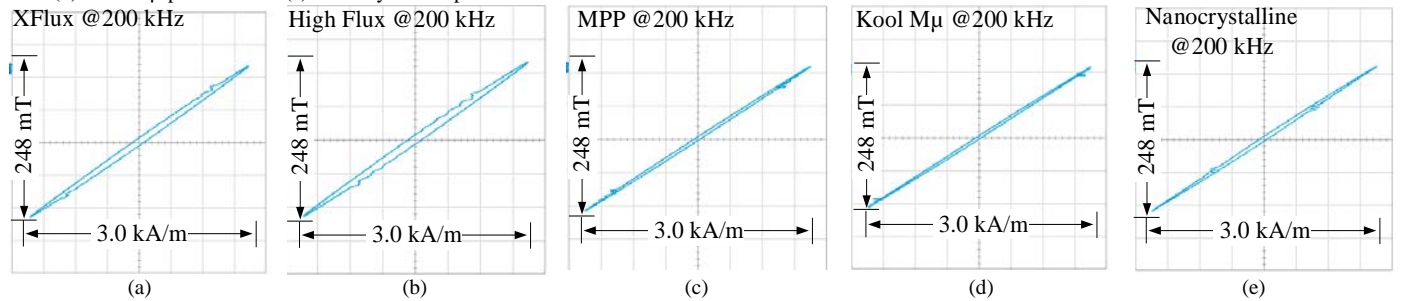


Fig. 9. Measured B-H curves with flux density of 248 mT under the frequency of 200 kHz. (a) X flux powder core. (b) High flux powder core. (c) MPP powder core. (d) Kool Mμ powder core. (e) Nanocrystalline powder core.

The measured voltage and current waveforms of the nanocrystalline core based inductors are shown in Fig. 7 with different currents from 2.26 to 9.1 A peak-to-peak AC excitations. Typically, due to the low relative permeability, low flux density will be resulted even though the AC current is high. This can benefit in enhancing the DC average output current within the demanded AC ripple. The B-H curves are calculated and plotted by using the B-H measurement toolbox from the LeCroy oscilloscope. The aim is to evaluate the response of the nanocrystalline powder core responding to an external magnetic field. As shown in Fig. 8, Fig. 9, and Fig. 10, the B-H curves of five powder cores are plotted at the operating frequencies of 100 kHz, 150 kHz, and 200 kHz when the peak-to-peak value of the AC excitation current is set at 9.1 A and the flux density is 248 mT. Among these B-H curves, the horizontal scale is set at 420 A/m and the vertical scale is set at 53 mT/div. It can be found that the magnetic hysteresis loops, dictated by the coercive force of MPP core, Kool Mμ core, and nanocrystalline core are much smaller than those of X flux core and high flux core. When the operating frequency is set at 100 kHz and the flux density peak value is set at 248 mT, the core losses of High flux core, X Flux core, MPP core, Kool Mμ core, and

nanocrystalline core are 75.6 W, 67.9 W, 32.4 W, 25.4 W, and 38.2 W, respectively. Furthermore, when the operating frequency is 200 kHz and the flux density is 248 mT (peak-to-peak), the core losses of High flux core, X flux core, MPP core, Kool M $\mu$  core, and nanocrystalline core are 171 W, 149 W, 70 W, 59 W, and 81 W, respectively. As shown in Fig. 10 and 12, the core loss increase of High Flux, X Flux, MPP, Kool M $\mu$  and nanocrystalline cores are 26%, 19%, 16%, 32% and 12% when the frequency changes from 100 kHz to 200 kHz.

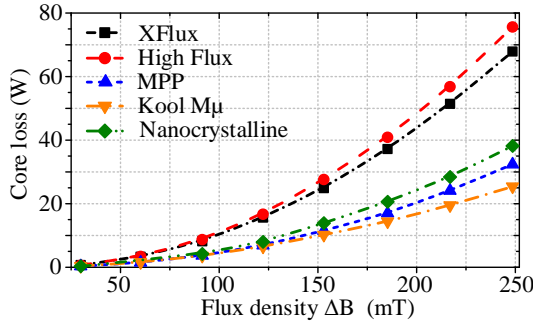


Fig. 10. Measured core loss of different cores at different  $\Delta B$  values when the operating frequency is 100 kHz.

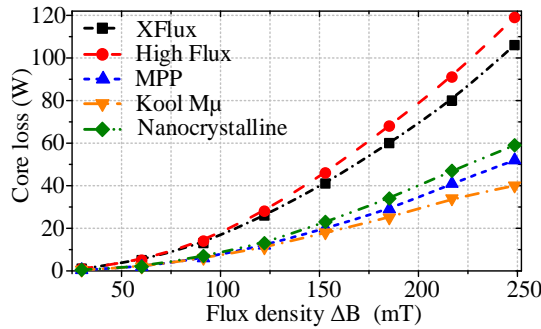


Fig. 11. Measured core loss of different cores at different  $\Delta B$  values when the operating frequency is 150 kHz.

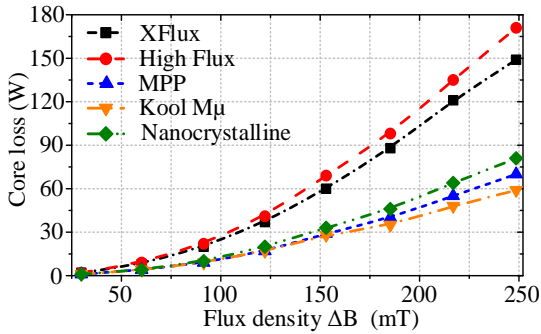


Fig. 12. Measured core loss of different cores at different  $\Delta B$  values when the operating frequency is 200 kHz.

The Kool M $\mu$ , MPP and the nanocrystalline powder cores have shown significantly fewer losses than the High Flux and X Flux powder cores thus those three powder cores are taken to higher operating frequencies up to 600 kHz. The AC sinusoidal current has a peak-to-peak value of 2.8 A which generates 75 mT flux density in the core. As shown in Fig. 13, the core loss deviation of the above three cores are not distinct before reaching 450 kHz. At 600 kHz, it can be found that the Kool

M $\mu$  presents the highest core loss of 56 W, nanocrystalline powder core has 53 W loss while the MPP presents the lowest core loss of 50 W.

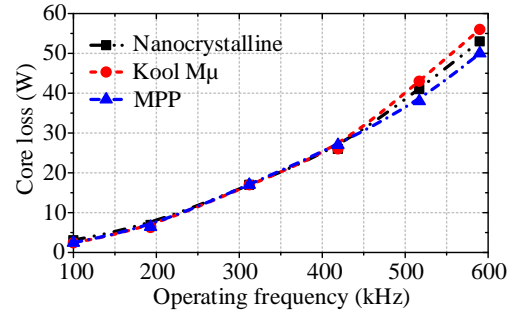


Fig. 13. Measured core loss at different operating frequencies when the peak-to-peak value of AC sinusoidal current is 2.8 A for 75 mT.

The thermal images of inductors using different cores under the same operation are provided as shown in Fig. 14, where the points of temperature taken from the core and winding are cross referred between the thermal and photographed images. It can be found that the core temperature is normally several degrees higher than the winding temperature. The visual deviation of temperature distribution between cores is due to emissivity, especially for the copper Litz wire with a thermally reflective surface where the emissivity is reduced. When the thermal camera is at different positions, the emissivity and reflectivity will have a slight variation, leading to uneven temperature distribution on the thermal image. Nevertheless, the qualitative comparisons among the powder cores are not affected. As shown in the result, the MPP core can reach the maximum temperature of 60.5 °C while the nanocrystalline core and Kool M $\mu$  core are 63.6 °C and 67.7 °C, respectively. These thermal results agree with the conclusion from measured core losses.

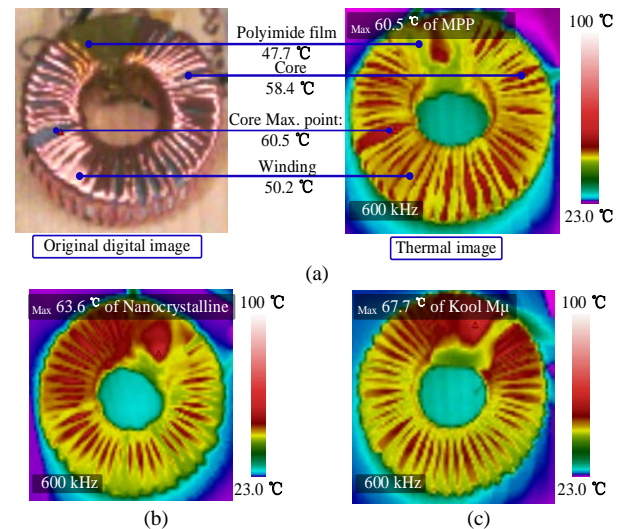


Fig. 14. Thermal effects with peak-to-peak AC sinusoidal current of 2.8 A under the frequency of 600 kHz. (a) MPP powder core. (b) Nanocrystalline powder core. (c) Kool M $\mu$  powder core.

Thus, it can be concluded that the MPP has the best performance with the lowest core loss when the operating



frequency is high. The nanocrystalline has a moderate core loss, which is better than Kool M $\mu$  at high frequency operation, more than 450 kHz, but worse than MPP. However, the cost of MPP core is much higher than nanocrystalline due to the use of Molybdenum. Considering both the core loss and cost, the nanocrystalline powder core is competitive in high frequency and high power applications.

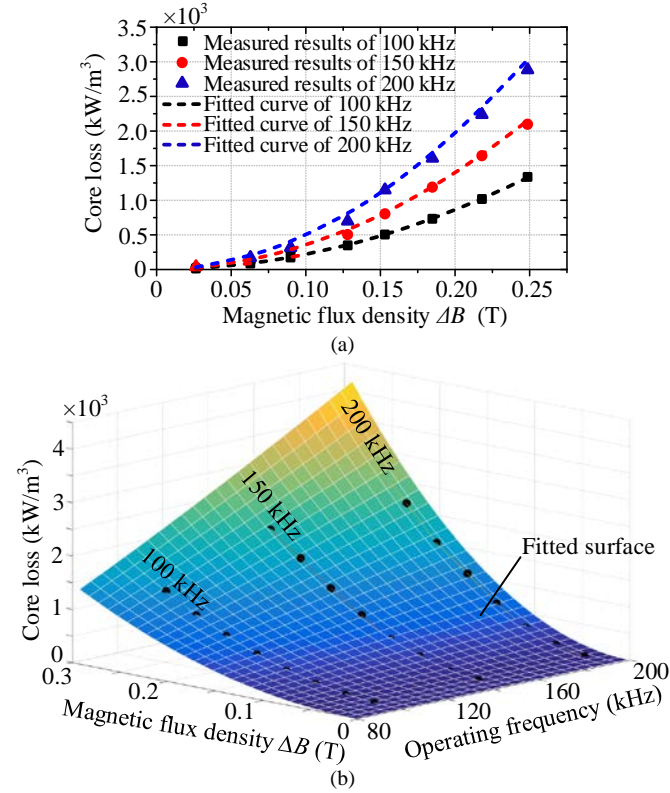


Fig. 15. Core loss with respect to different flux densities and Steinmetz parameter determination of nanocrystalline powder toroidal core. (a) Fitted curves. (b) Fitted surface.

## B. Steinmetz Parameters Determination

According to (2) and the measured results, the Steinmetz parameters  $k_i$ ,  $\alpha$ , and  $\beta$  can be determined by using the curve fitting tool. The Steinmetz equation is set by the MATLAB curve fitting tool as the target equation and the measured operating frequency, flux density, and core loss are fed into the tool to extract the Steinmetz parameters. As a result,  $k_i$ ,  $\alpha$ , and  $\beta$  are determined to be 89.38, 1.193, and 2.01, respectively. Thus, the core loss of the nanocrystalline powder core is linear with  $f^{1.193}$  and  $B^{2.01}$ . As shown in Fig. 15 (a), the fitted curves are well-matched with the measured core loss points. Moreover, the core loss surface of the nanocrystalline powder core has been plotted with respect to various flux densities and operating frequencies based on the Steinmetz equation (2), as shown in Fig. 15 (b). Therefore, the core loss of the nanocrystalline powder inductor can be easily calculated from 80 kHz to 200 kHz at different flux densities.

## C. Thermal Effect under Sinusoidal AC Excitation

To evaluate the temperature and heat distribution of the powder cores under high-frequency and high flux density operations, the thermal images of the five powder cores are recorded as shown in Fig. 16, and Fig. 17, which are corresponding to the peak-to-peak AC sinusoidal current of 5.66 A and 8.49 A at the thermal steady state. All thermal images are captured by the thermal imaging camera FLIR E53 with more than 43,200 points of temperature measurement and  $240 \times 180$  pixels resolution.

It should be noticed that At the operating frequency of 200 kHz, it can be found that the temperature of the high flux core can reach up to 109 °C, which is the highest when the operating frequency is 200 kHz and the  $\Delta B$  is 233 mT. The thermal results of the five cores agree with the measured results of magnetic losses, the Kool M $\mu$  core has the lowest core loss and the lowest temperature at 200 kHz.

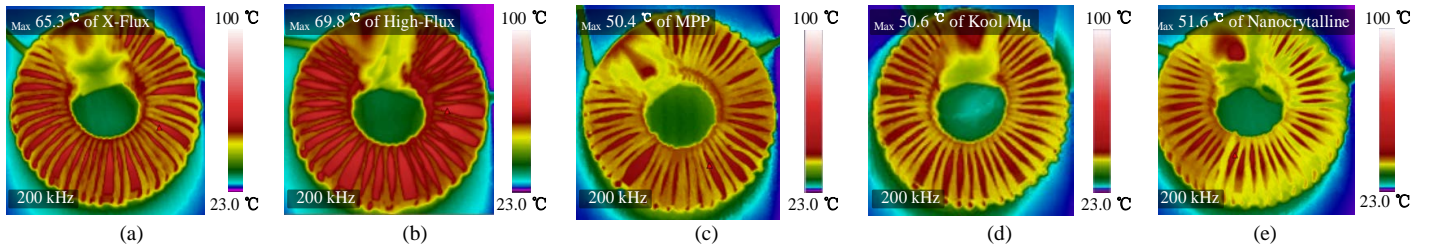


Fig. 16. Thermal effects with peak-to-peak AC sinusoidal current of 5.66 A under the frequency of 200 kHz. (a) X flux powder core. (b) High-flux powder core. (c) MPP powder core. (d) Kool M $\mu$  powder core. (e) Nanocrystalline powder core.

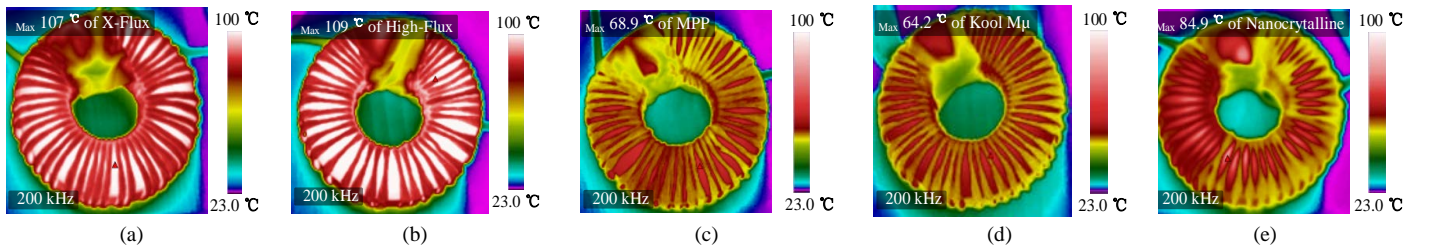


Fig. 17. Thermal effects with peak-to-peak AC sinusoidal current of 8.49 A under the frequency of 200 kHz. (a) X flux powder core. (b) High-flux powder core. (c) MPP powder core. (d) Kool M $\mu$  powder core. (e) Nanocrystalline powder core.



## V. CONCLUSION

In this paper, a soft magnetic composite based nanocrystalline powder core is fabricated, examined and verified, which can be applied for high power inductors. The evenly distributed air gaps of a nanocrystalline powder core eliminate the gap loss problems associated with gapped ferrite cores and nanocrystalline ribbon cores. The magnetic properties have been experimentally investigated and compared with other four commercially available powder cores: X Flux, High Flux, Kool M $\mu$  and MPP cores. Experimental validation includes core loss measurement, DC bias measurement, and thermal performance analysis. As a result, the new nanocrystalline powder core has a slightly compromised loss and performance than the MPP and Kool M $\mu$  below the operating frequency of 200 kHz. However, the nanocrystalline powder core is more competitive at higher operating frequencies of more than 450 kHz.

## REFERENCES

- [1] R. M. Burkart, and J. W. Kolar, "Comparative  $\eta$ - $p$ - $\sigma$  pareto optimization of Si and SiC multilevel dual-active-bridge topologies with wide input voltage range," *IEEE Transactions on Power Electronics*, vol. 32, no. 7, pp. 5258-5270, July, 2017.
- [2] M. Cupelli, S. K. Gurumurthy, S. K. Bhandari, Z. Yang, P. Joeiges, A. Monti, and R. W. De Doncker, "Port controlled hamiltonian modelling and IDA-PBC control of dual active bridge converters for dc microgrids," *IEEE Transactions on Industrial Electronics*, vol. 66, no. 11, pp. 9065 - 9075, Nov., 2019.
- [3] B. Zhao, Q. Song, W. Liu, and Y. Sun, "Overview of dual-active-bridge isolated bidirectional dc-dc converter for high-frequency-link power-conversion system," *IEEE Transactions on Power Electronics*, vol. 29, no. 8, pp. 4091-4106, Aug., 2014.
- [4] M. G. S. Pearce, G. A. Covic, and J. T. Boys, "Robust ferrite-less double D topology for roadway IPT applications," *IEEE Transactions on Power Electronics*, Nov., 2018.
- [5] C. C. Mi, G. Buja, S. Y. Choi, and C. T. Rim, "Modern advances in wireless power transfer systems for roadway powered electric vehicles," *IEEE Transactions on Industrial Electronics*, vol. 63, no. 10, pp. 6533-6545, Oct., 2016.
- [6] C. Jiang, K. T. Chau, C. H. T. Lee, W. Han, W. Liu, and W. H. Lam, "A wireless servo motor drive with bidirectional motion capability," *IEEE Transactions on Power Electronics*, DOI: 10.1109/TPEL.2019.2904757, 2019.
- [7] L. Dorn Gomba, P. Magne, B. Danen, and A. Emadi, "On the concept of the multi-source inverter for hybrid electric vehicle powertrains," *IEEE Transactions on Power Electronics*, vol. 33, no. 9, pp. 7376-7386, Sept., 2018.
- [8] L. Tan, B. Wu, S. Rivera, and V. Yaramasu, "Comprehensive DC power balance management in high-power three-level dc-dc converter for electric vehicle fast charging," *IEEE Transactions on Power Electronics*, vol. 31, no. 1, pp. 89-100, Jan., 2016.
- [9] G. R. C. Mouli, J. Schijffelen, M. van den Heuvel, M. Kardolus, and P. Bauer, "A 10 kW solar-powered bidirectional EV charger compatible with chademo and combo," *IEEE Transactions on Power Electronics*, vol. 34, no. 2, pp. 1082-1098, Feb., 2019.
- [10] J. Millán, P. Godignon, X. Perpiñà, A. Pérez-Tomás, and J. Rebollo, "A survey of wide bandgap power semiconductor devices," *IEEE transactions on Power Electronics*, vol. 29, no. 5, pp. 2155-2163, May, 2014.
- [11] S. D. Sudhoff, *Power magnetic devices: A multi-objective design approach*: John Wiley & Sons, 2014.
- [12] R. Kubacki, J. Ferenc, R. Przesmycki, and M. Wnuk, "The nanocrystalline FeSiBCuNb Finemet absorption properties at microwaves," *IEEE Transactions on Electromagnetic Compatibility*, vol. 54, no. 1, pp. 93-100, Jan., 2012.
- [13] J. Wang, K. J. Dagan, X. Yuan, W. Wang, and P. H. Mellor, "A practical approach for core loss estimation of a high-current gapped inductor in pwm converters with a user-friendly loss map," *IEEE Transactions on Power Electronics*, vol. 34, no. 6, pp. 5697-5710, June, 2019.
- [14] J. Imaoka, K. Okamoto, M. Shoyama, Y. Ishikura, M. Noah, and M. Yamamoto, "Modeling, magnetic design, simulation methods, and experimental evaluation of various powder cores used in power converters considering their dc superimposition characteristics," *IEEE Transactions on Power Electronics*, vol. 34, no. 9, Sept., 2019.
- [15] W. M. Wang, K. W. E. Cheng, K. Ding, and T. F. Chan, "A polymer-bonded magnetic core for high-frequency converters," *IEEE Transactions on Magnetics*, vol. 48, no. 11, pp. 4328-4331, Nov., 2012.
- [16] A. Hilal, M. A. Raulet, C. Martin, and F. Sixdenier, "Power loss prediction and precise modeling of magnetic powder components in DC-DC power converter application," *IEEE Transactions on Power Electronics*, vol. 30, no. 4, pp. 2232-2238, April, 2015.
- [17] J. Muhlethaler, J. Biela, J. W. Kolar, and A. Ecklebe, "Improved core-loss calculation for magnetic components employed in power electronic systems," *IEEE Transactions on Power Electronics*, vol. 27, no. 2, pp. 964-973, Feb., 2012.
- [18] Y. R. Wang, G. Calderon Lopez, and A. J. Forsyth, "High-frequency gap losses in nanocrystalline cores," *IEEE Transactions on Power Electronics*, vol. 32, no. 6, pp. 4683-4690, Jun, 2017.
- [19] W. Shen, F. Wang, D. Boroyevich, and C. W. Tipton, "High-density nanocrystalline core transformer for high-power high-frequency resonant converter," *IEEE Transactions on Industry Applications*, vol. 44, no. 1, pp. 213-222, Jan.-Feb., 2008.
- [20] J. Fuzer, S. Dobak, and P. Kollar, "Magnetization dynamics of fecunbsib soft magnetic ribbons and derived powder cores," *Journal of Alloys and Compounds*, vol. 628, pp. 335-342, Apr 15, 2015.
- [21] M. Soinski, J. Leszczynski, C. Swieboda, and M. Kwiecien, "Nanocrystalline block cores for high-frequency chokes," *IEEE Transactions on Magnetics*, vol. 50, no. 11, pp. 2801904: 1-4, Nov., 2014.
- [22] X. Wang, Z. Lu, C. Lu, and D. Li, "Fe-based nanocrystalline powder cores with ultra-low core loss," *Journal of Magnetism and Magnetic Materials*, vol. 347, pp. 1-3, Dec., 2013.
- [23] Y. Yoshizawa, S. Oguma, and K. Yamauchi, "New Fe-based soft magnetic alloys composed of ultrafine grain structure," *Journal of Applied Physics*, vol. 64, no. 10, pp. 6044-6046, Nov., 1988.
- [24] D. Nuetzel, G. Rieger, J. Wecker, J. Petzold, and M. Mueller, "Nanocrystalline soft magnetic composite-cores with ideal orientation of the powder-flakes," *Journal of Magnetism and Magnetic Materials*, vol. 196-197, pp. 327-329, May, 1999.
- [25] H. P. Kronmüller, Stuart; Herzer, Giseler, *Soft magnetic materials—nanocrystalline alloys*: John Wiley & Sons, 2007.
- [26] C. Wu, H. Chen, H. Lv, and M. Yan, "Interplay of crystallization, stress relaxation and magnetic properties for FeCuNbSiB soft magnetic composites," *Journal of Alloys and Compounds*, vol. 673, pp. 278-282, Mar., 2016.
- [27] T. Hatakeyama, and K. i. Onda, "Core loss estimation of various materials magnetized with the symmetrical/asymmetrical rectangular voltage," *IEEE Transactions on Power Electronics*, vol. 29, no. 12, pp. 6628-6635, Dec., 2014.
- [28] M. Mu, Q. Li, D. J. Gilham, F. C. Lee, and K. D. Ngo, "New core loss measurement method for high-frequency magnetic materials," *IEEE Transactions on Power Electronics*, vol. 29, no. 8, pp. 4374-4381, Aug., 2014.
- [29] H. Zhao, C. Ragusa, C. Appino, O. Barriere, Y. Wang, and F. Fiorillo, "Energy losses in soft magnetic materials under symmetric and asymmetric induction waveforms," *IEEE Transactions on Power Electronics*, vol. 34, no. 3, pp. 2655-2665, Mar., 2019.
- [30] S. Barg, K. Ammous, H. Mejibri, and A. Ammous, "An improved empirical formulation for magnetic core losses estimation under nonsinusoidal induction," *IEEE Transactions on Power Electronics*, vol. 32, no. 3, pp. 2146-2154, Mar. 2017.
- [31] H. Matsumori, T. Shimizu, K. Takano, and H. Ishii, "Evaluation of iron loss of ac filter inductor used in three-phase PWM inverters based on an iron loss analyzer," *IEEE Transactions on Power Electronics*, vol. 31, no. 4, pp. 3080-3095, Apr., 2016.
- [32] Y. Zhang, P. Sharma, and A. Makino, "Fe-rich Fe-Si-B-P-Cu powder cores for high-Frequency power electronic applications," *IEEE Transactions on Magnetics*, vol. 50, no. 11, pp. 2006804:1-4, Nov., 2016.



**Chaoqiang Jiang** (S'16, M'19) received the B.Eng. and M.Sc. degrees in electrical engineering and automation from Wuhan University, Wuhan, China, in 2012 and 2015, respectively, and the Ph.D. degree in electrical and electronic engineering from The University of Hong Kong, Hong Kong, in 2019.

He is currently a Postdoctoral Research Associate at the University of Cambridge, U.K. In 2019, he was a Visiting Researcher at the Nanyang Technological University, Singapore. His current research interests include power electronics, wireless power transfer techniques, electric machines and drives, and electric vehicle (EV) technologies.



**Hui Zhao** (S'14, M'18) received the bachelor and master degrees in electrical engineering from Huazhong University of Science and Technology, Wuhan, China, in 2010 and 2013, respectively, and the Ph.D. degree in power electronics from the University of Florida, Gainesville, FL, USA, in 2018.

He had a Summer Internship with General Electric Global Research Center, Shanghai, in 2013. He is currently a Postdoctoral Research Associate with the University of Cambridge, Cambridge, UK. His research interests include the modeling and driving of the power devices, EMI, and the high power density power converters.



**Xinru Li** (S'17) received the B.Eng. Degree in Materials Science and Engineering from University of Science and Technology Beijing (USTB), China in 2017. In 2019, he received the M.Phil. Degree in Electrical Engineering from the University of Cambridge, United Kingdom.

He is currently a Ph.D. research student at the Department of Engineering, University of Cambridge. His research interests include magnetic materials, particularly for power electronics application, wireless charging systems and high-frequency transformers.



**Yanfeng Shen** (S'16, M'18) received the B.Eng. degree in electrical engineering and automation and the M.Sc. degree in power electronics from Yanshan University, Qinhuangdao, China, in 2012 and 2015, respectively, and the Ph.D. degree in power electronics from Aalborg University, Aalborg, Denmark, in 2018.

He is currently a Postdoctoral Research Associate at the University of Cambridge, UK. He worked as an Intern with ABB Corporate Research Center, Beijing, China, in 2015. He was a Visiting Graduate Research Assistant with Khalifa University, UAE, in 2016. His current research interests include the thermal management and reliability of power electronics, electric vehicle (EV) traction inverters, and applications of SiC and GaN power devices.



**Saikat S. Ghosh** (S'18) received his BE from Indian Institute of Engineering Science and Technology, Shibpur, India in 2011, and the ME degree in 2013 from the Indian Institute of Science, India. After a two year career as Manager, at Engineering Research Centre of Tata Motors Ltd he joined the University of Cambridge, Engineering Department in 2015.

After finishing his PhD in 2019, he joined AVL powertrain UK Ltd and currently working as a system engineer there. His research interests include automotive electrification system design, particularly power electronics converters and high-frequency converters using wide band gap materials for automotive application.



**Teng Long** (M'13) received the B.Eng. degree from the Huazhong University of Science and Technology, China, the first class B.Eng. (Hons.) degree from the University of Birmingham, UK in 2009, and the Ph.D. degree from the University of Cambridge, UK in 2013.

Until 2016, he was a Power Electronics Engineer with the General Electric (GE) Power Conversion business in Rugby, UK. He is currently a Lecturer with the University of Cambridge. His research interests include power electronics, electrical machines, and machine drives. Dr Long is a Chartered Engineer (CEng) registered with the Engineering Council in the UK.